Joint Institute for Nuclear Research

2 T Superconducting Detector Solenoid for the PANDA Target Spectrometer
Part 1
Conceptual Design of the Solenoid Magnet

Dubna
2007

I. INTRODUCTION

An important component of the FAIR GSI facility in Darmstadt, Germany, is the High Energy Storage Ring (HESR), which is dedicated to collisions of antiprotons with momentum up to 15 GeV/c with various targets. The structure of hadrons in the charmonium mass range and spectroscopy of hypernuclei have to be investigated at this facility. This physics program will be realized at a general purpose detector called PANDA. Having high rates (10^7 annihilations/sec), with good particle identification and momentum resolution for γ, ε, μ, π, K and p, this detector facility will have various internal targets available.

According to "Conceptual Design and Simulation of the Panda Detector" [1], the PANDA experimental facility at HESR will include a target spectrometer with a 2 T superconducting solenoid. A preliminary design concept of the solenoid elaborated by JINR team was reported in [2]. The latest modifications of the solenoid design are reported in this paper.

II. REQUIREMENTS FOR THE SOLENOID

The solenoid layout is shown in Fig. 1. As it can be seen from the picture, all main detectors of the PANDA spectrometer are placed inside the solenoid coil. Thus the requirement of the cryostat radiation transparency is not as strong as that for large detector solenoids with an aluminium stabilized superconductor [3], [4], [5], [6]. The cryostat must be sufficiently transparent for muon detection only.

The inner dimensions of the solenoid cryostat and its length are defined by the arrangement of the central detectors (vertex detector, outer tracker, particle identification system, electromagnetic calorimeter, Cherenkov detector). The muon detectors are planned to be allocated inside lamination of the flux return yoke and on its inner surface.
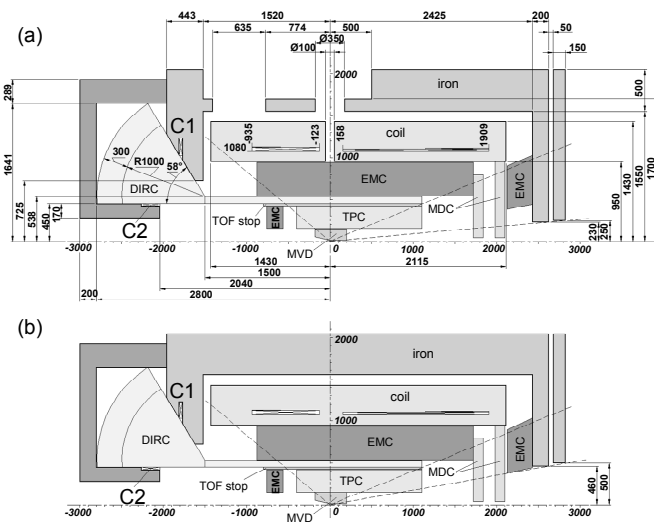

Fig. 1. PANDA solenoid layout. a) Side view, b) Top view.

The main requirements for the solenoid in respect to the detector systems are:

- Magnetic field of 2 T in the area of the tracker;
- Field inhomogeneity better than 1.7 % in the tracker area (Straw detector option);
- Homogeneity of the radial component of the magnetic field induction: $\int B_r\, dz / B_{0S} < 2\,mm$ (B_{0S} is the average induction in the tracker volume in case of Charged Particle Tracker (TPC) option)
- The stray field in the area of the Photo Multiplier Tubes (PMT) of the Cherenkov Detector (DIRC): < 1 mT.

TABLE I
SOLENOID FIELD REQUIREMENTS

Criteria	Absolute value	Base
Homogeneity over outer tracker region -0.4m < z < 1.1m, 0.15m< r <0.42m		
$\Delta B/B_{0s}$ < 1.7 %	$\Delta B = (B_{max}-B_{min})/2$	$B_{0s} = \int Bdv/V$ V -volume of the straw tracker
Homogeneity over vertex tracker region -0.1m < z < 0.2m, 0 < r < 0.12 m		
$\Delta B/B_{0v}$ < 1.7%	$\Delta B = (B_{max}-B_{min})/2$	$B_{0v} = \int Bdv/V_v$ V_v -volume of the Vertex
Homogeneity over a cylindrical layer of the outer tracker 0.15m <r <0.42m		
IntBr1/B_{0s}<2mm IntBr2/B_{0s}<2mm	$IntBr1 = \int_{-0.4}^{z} B_r dz$ $IntBr2 = \int_{z}^{1.1} B_r dz$	$B_{0s} = \int Bdv/V$ V -volume of the straw tracker
The stray fields in the area of Photo Multiplier Tubes of DIRC Z_0 = -1.5 m, R_0 =0.538 m, 1 m <ρ < 1.3 m 0< φ < 58°		
B < 1 mT		

These field requirements are summarized in Table I.
There are some additional requirements:

- The 17 ton Electromagnetic Calorimeter (EMC) must be attached to the inner surface of the cryostat shell;
- The iron yoke should hold the cryostat weight;
- The unbalanced axial forces applied to the coil should be transmitted to the yoke upstream end cap;
- A warm hole of 100 mm in diameter between the unequal coil parts should be made as well as the hole of 350 mm in the barrel part of the yoke for the Cluster Target System accommodation;
- The downstream door of the yoke should be sliding to provide access to the inner detectors. It is mounted on the skids;
- The solenoid has to be mounted on a movable rail-guided carriage to be transported from the assembly area to its operational position;
- All the cryogenic equipment mounted on the cryostat top has to be allocated in the upstream part to liberate the maximal space for target devices.

The superconducting solenoid must be assembled at the first place to provide support of all inner detectors.

III. CONSTRUCTION OF SOLENOID

A. Solenoid Design

The PANDA solenoid is a magnet with a thin superconducting NbTi winding and flux return yoke, as shown in Fig. 2. The solenoid winding is housed in the stainless steel cryostat. A warm hole of 100 mm in diameter is located between the solenoid subcoils. The flux return yoke consists of an octagonal barrel and two end caps. The
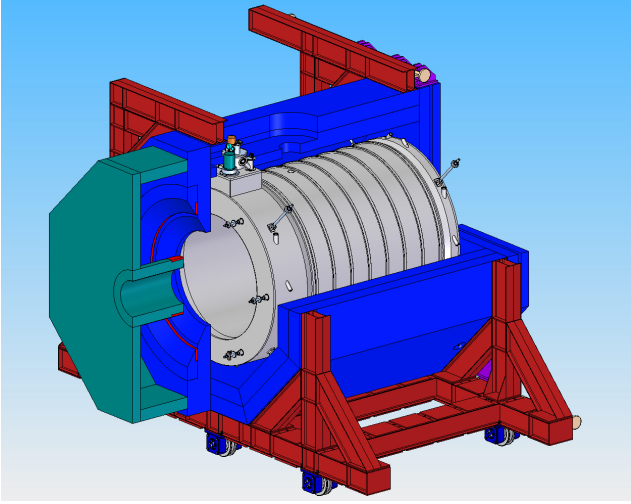

Fig. 2. 3D view of the PANDA solenoid.

downstream end cap is sliding to provide access to detectors.

Fig. 3 shows the longitudinal cross section of the PANDA superconducting solenoid with the dimensions of the cryostat, of the superconducting coil and iron yoke. The main
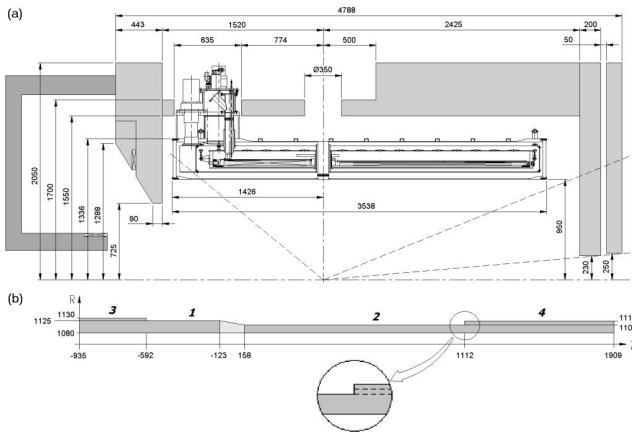

Fig. 3. SC solenoid. a) Solenoid longitudinal cross section, b) Coil dimensions.

dimensions of the magnet are summarized in Table II.

B. Magnetic field and forces calculations

TOSCA [7] simulations have been performed to calculate magnetic fields and forces acting on the solenoid coils and iron yoke.

TABLE II. MAIN DIMENSIONS OF THE CRYOSTAT AND OF THE IRON YOKE

Cryostat	
Inner radius (warm hole), m	0.950
Outer radius, m	1.336
Length, m	3.637
Forward length (z^-), m	1.426
Backward length (z^+), m	2.211
Iron Yoke	
Incircle radius of the yoke, m	1.550
Circumcircle radius of the yoke, m	2.219
Length of the yoke, m	4.788

The superconducting coil with an average current density of $6.2 \cdot 10^7$ A/m^2 was designed to achieve the required magnetic flux density of 2.0 T in the tracker area. The peak of magnetic field induction in the coil is 2.96 T.

The distribution of magnetic induction in the area of the tracker is presented in Fig. 4. An acceptable level of field inhomogeneity of 1.7 % in the tracker area is provided by means of correcting coils 3 and 4 placed on the outer surface of the main coils. The correcting coils compensate the local magnetic field inhomogeneity resulting from initial design
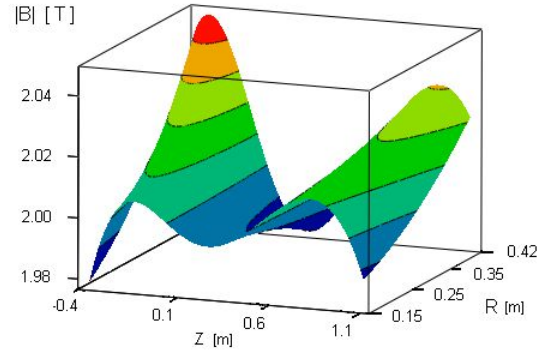

Fig. 4. Distribution of the magnetic induction in the area of tracker.

constraints on the solenoid length.

Application of TPC instead of the Straw detector for the tracker would assume that the integral of the radial component of the magnetic field has to be constrained (see Table I). Distribution of the integral of the radial component over the region of the Charged Particle Tracker (TPC) $\int B_r \, dz / B_{0S}$ is presented in Fig. 5 (for two different positions of the readout plane: upstream and downstream). It can be seen from the picture that the normalized integral doesn't exceed 2 mm.

The field homogeneity and the integral of the radial component of the magnetic field as well as the axial component of the magnetic force applied to the coil, are very

sensitive to the axial position of the coil with respect to the return yoke. The axial force acting on the solenoid coil, the integral of the radial component and field inhomogeneity in the tracker area versus the coil displacement in axial direction, are shown in Fig. 6. The nominal values of the axial force, integral of the radial component of induction and field inhomogeneity at the initial coil position, are as follows:

- Axial magnetic force $F_z = 121$ kN
- Integral of radial component $I = \int B_r \, dz = 39$ Gm
- Field inhomogeneity $\delta = \Delta B/B = 1.7$ %

Axial displacement ±1 cm of the coil results in the following deviations: $\Delta F_z = \pm 91$ kN; $\Delta I = \pm 1$ Gm; $\Delta \delta = \pm 0.15$ %.
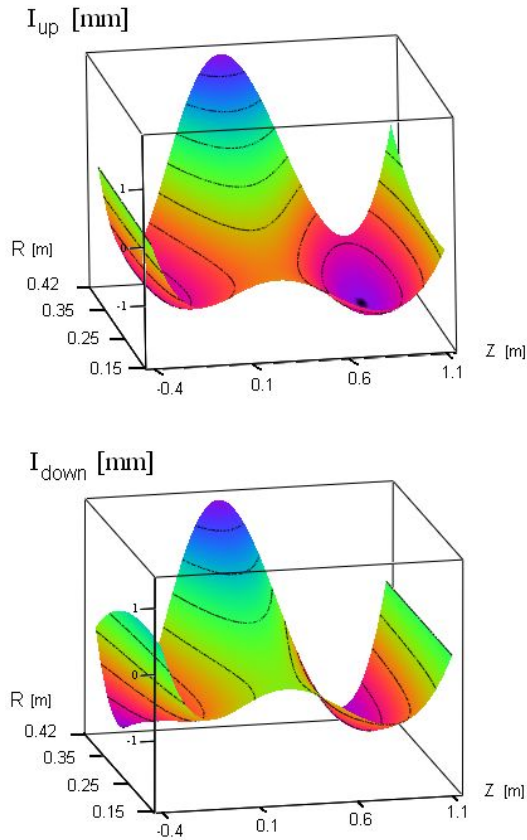
Fig. 5. Distribution of integral of the radial component over region of the tracker $\int B_r dz / B_{0s}$. a) Upstream readout plane, b) Downstream readout plane.

There are recesses in the iron at outer surfaces of the top and bottom beams for the target accommodation (Fig. 3a). The local thinning of the return yoke caused by these recesses, doesn't influence considerably the stray fields on the outside surface of the yoke in the area of the target equipment. The magnetic field in this area is < 5 mT. To compensate the decrease of barrel magneto conductivity due to thinning of the yoke for target accommodation, the thickness of beams was increased.

The integral of the normal component of the magnetic induction along the straight track line from the origin (0,0) and directed to 22° from Z-axis up to the end of the outer tracker, is shown in Fig. 7.
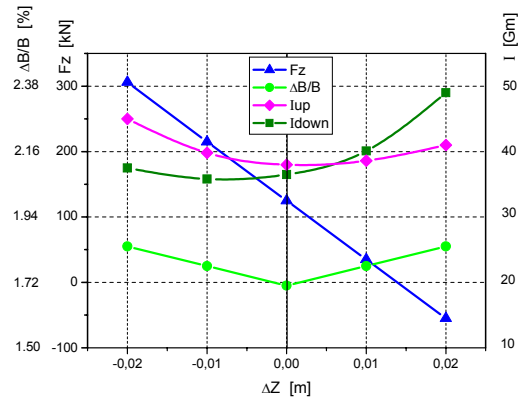
Fig. 6. Axial force Fz, integral of the radial component and the field inhomogeneity ΔB/B in the tracker area versus coil axial displacement

Deviation of the solenoid coil axis by the angle of 1° from Z-axis causes a torque of 3.5 kN·m applied to the coil. A radial displacement of the coil by 1 cm with respect to the yoke, produces a radial offset force of 32 kN.
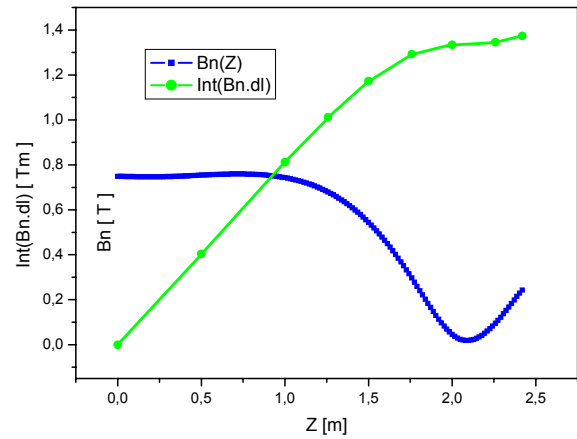
Fig. 7. The integral of normal component of the magnetic induction along the straight track line of 22°

Distributions of the equivalent radial pressure and of the axial force density characterizing concentration of the axial magnetic force along the coil axis, are shown in Fig. 8. The axial attraction force between the both parts of the coil is about 3.5 MN. The maximum radial pressure is about
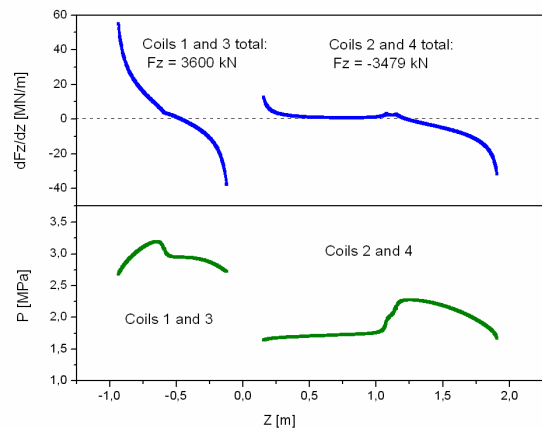
Fig. 8. Distribution of the axial force density and radial pressure.

3.2 MPa.

The thick-walled magnetic shield and trim coils c1 and c2 in the solenoid upstream area have been applied to suppress stray fields in the area of DIRC PMT's.

The position of the upstream end cap above the water tank of DIRC (Fig.3) is the compromise between minimization of the integral of radial component of the induction and stray fields in the area of DIRC PMT from one side, and minimization of the axial magnetic force applied to the solenoid coil, – from the other side. This is true for the given DIRC silica crystal stack length. It is important to have a positive axial force direction, since the axial tie rods have to be placed in the upstream area not to interfere with the backward EMC and DIRC. The magnetic field distribution in the area of DIRC PMT is given in Fig. 9. The stray fields do not exceed the acceptable level of 1 mT in this area. The 1 cm layer of pure iron on the inner surface of the shield can
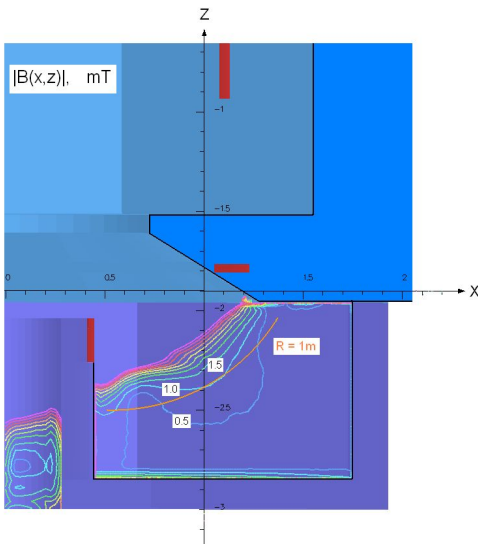

Fig. 9. Stray field in the DIRC PMT region

additionally reduce the stray field by 12%.

The magnetic circuit of the solenoid is not saturated. The current density dependence of the solenoid central field is almost linear and the curve of the axial force is close to the
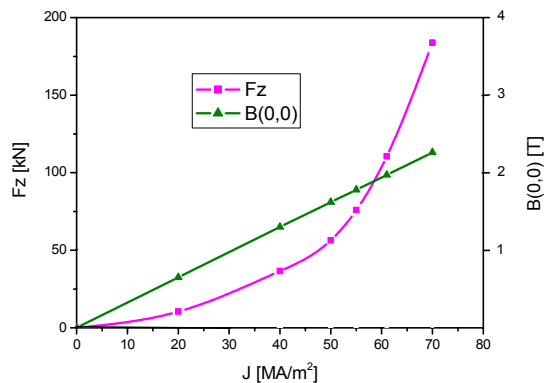

Fig. 10.Solenoid central magnetic field and axial force versus current density.

quadratic one (see Fig. 10).

The stray field at a radial distance of 4 m from the magnet system (solenoid + dipole) does not exceed 3 mT [2]. The

TABLE III
MAIN PARAMETERS OF THE SOLENOID

Ampere-turns of the solenoid, MA	5.79
Nominal operational current, kA	2.05
Design current density (without ground wall insulation), MA/m^2	62
Stored energy, MJ	22.3
Self inductance, H	10.6
Maximum induction in the superconducting winding, T	2.96

main parameters of the solenoid are given in Table III.

C. Conductor

Wire-in-channel conductor

To reduce costs of the conductor and simultaneously increase the lengths of its pieces, it is planned to use a wire-in-channel type of the conductor. This solution will reduce the number of joints in the solenoid and provide a high copper content for the sake of stability and safety.

The operational current of the solenoid is 2050 A. The conductor (Fig. 11) consists of a superconductor flat Rutherford cable soldered in a C-form beam profile (4 mm×7 mm) made of high purity copper. The flat cable is braided of 13 superconducting strands 0.5 mm in diameter
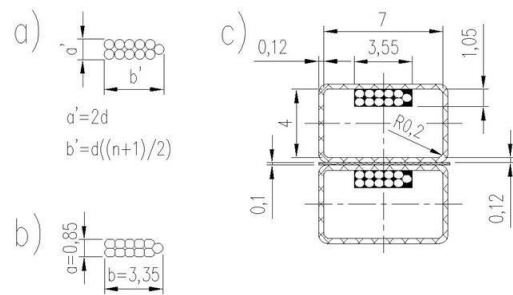
Fig. 11. PANDA superconductor

having 60 superconducting filaments, each 42 μm in diameter. The Cu:SC ratio is 1.3/1. The main design parameters of the copper matrix and the superconducting cable are summarized in Table IV.

At the temperature of 4.2 K and magnetic field of 2.96 T a single wire bears the current of 310 A. The total current for 13 strands cable is 13 x 310 = 4030 A. Thus it is enough to ensure the chosen safety factor of 2.

The sizes of the flat cable before pressing are defined as shown in Fig. 11a: a' = 2d and b' = (n+1)d/2 [8]. After pressing the final dimensions of the cable should be: a=2d-ε_a and b=(n+1)d/2 − ε_b, where ε_a = (0.3 ± 0.1)d and ε_b = (0.3±0.1)d (Fig. 11b). So, the final sizes have been chosen: a = 0.85 mm and b = 3.35 mm. The fill factor of the metal in the flat cable

is about 90 %. The grove for the flat cable in the cooper channel has the following sizes: A = 1.05 mm and

TABLE IV
PARAMETERS OF THE SUPERCONDUCTING CABLE

C-form chanel	
Material	Cu (RRR 100)
Overall dimensions, mm^2	4 × 7
Groove for flat cable, mm^2	1.05 × 3.55
SC insert	
Material	NbTi/Cu
Number of strands	13
Diameter of a strand, mm	0.5
Cu/NbTi ratio	1.3/1
Critical current (B= 2.96T, T=4.2K), A	4030
Number of filaments	60
Filament diameter, μm	42

B = 3.55 mm (Fig. 11*c*).

Insulation

It is planned to use a Kapton (polyimide) tape film wrapped spirally around the conductor and fused. The thickness of the film is about 0.012 mm. The dielectric strength of this insulation is of 110-175 kV/mm. Besides, the half lapped prepreg tape of 0.1 mm (after compression) is applied to bond the coil turns after a heating procedure for epoxy. The electrical strength of 1 mm layer of fiberglass ground wall insulation is 1 kV.

The final dimensions of the conductor array cell, which includes the conductor, turn-to-turn insulation and interlayer sheets (packing factor in axial directions 0.99), are 4.38 x 7.31 mm = 31.74 mm^2. The fill factors of the copper, insulation, superconductor and solder in the conductor cell are λ_{Cu} = 0.806, λ_{ins} = 0.122, λ_{sc} = 0.035 and λ_{sl} = 0.037, respectively. The total length of the conductor in the coil and its weight are 20 km and 5 ton, respectively.

Stability of the conductor

The distributed and point transient disturbance spectra have been considered for the solenoid conductor. The maximum energy density of large volume disturbances, supported by the solenoid without quench, is shown in Fig. 12 as a function of the magnet operation current divided by the critical current at 4.2 K. The maximum permitted energy density decreases very rapidly as I approaches Ic. Ratio I/Ic=0.5 has been chosen to have some margin against the large volume disturbances. In this case the coil parts can withstand a mutual axial inelastic movement of about 0.4 mm without quenching.
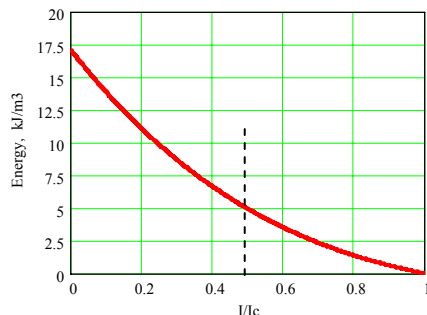

Fig. 12. Maximum energy density for a large volume disturbance supported by the superconductor cable as a function of the ratio current to critical current.

The approximate theory developed by Wilson [9] on the Minimum Propagating Zone (MPZ) has been adopted to analyze the solenoid behavior during a point disturbance. The critical temperature Tc is 8.04 K at J=0 and B=Bmax. The shearing temperature is 6.2K. The stability level against the point disturbances depends mainly on thermal and electrical properties of the copper matrix as well as on the cable size. For these reasons the minimum energy necessary to establish a three dimensional propagating zone, is presented in Fig. 13 for two different specific resistances of the copper matrix.
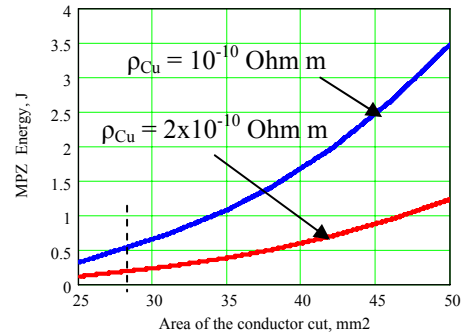

Fig. 13. Maximum energy needed to establish a minimum propagation zone (MPZ) as a function of the conductor area cut.

The MPZ energy is expressed as a function of the conductor area cross-section. It is clear that the copper specific resistance is a very critical parameter. The safety margin against point disturbances is reduced by a factor of about 2.8 when going from high purity copper (residual resistivity ratio RRR = 200 at B = 0) to copper (RRR=100 at B = 0).

If assuming that the point disturbance energy is of the order of 10 mJ - a typical value used for thin detector solenoids computations – and imposing a safety factor 100 against an accidental quench arising from incidental point disturbances, we can conclude that the value of RRR for the copper matrix should be greater than 200 and the copper channel dimensions of 5 mm x 7 mm have to be provided.

However, the safety factor 100 against the accidental quench has been chosen experimentally for thin solenoids with the aluminum conductor. In that type of winding there are significant values of mechanical shear stresses at the glued interface between the conductor and the support tube, which can be the source of the local heat release.

The shear stresses can be minimized in a winding by giving an opportunity to the whole winding body to separate from the coil form and take its natural shape while the magnet energizing. This type of windings is the so-called coreless coil [10].

Of course, it can't be applied to the aluminum stabilized coils of the detector magnets because of the high level of hoop stress in the conductor without an outer mandrel. But there are no principal objections to construct a detector magnet with a copper stabilized conductor if physical requirements don't

include radiation transparency of the cryostat. For example, the conductor of detector SLAC [11] has a copper matrix. This magnet has similar dimensions and parameters like the PANDA magnet and its superconducting winding has never quenched.

It is not clear how an additional stabilizer volume enhances the stability level of the conductor since the glue surfaces of the winding are increasing simultaneously and therefore the probability of a quench is increasing as well. Besides, the increase of stability level due to the current diffusion effect is not evident. So, expecting more auspicious mechanical stresses in a coreless winding, the conductor cross section of 4 mm x 7 mm (25.6 mm^2 of copper) has been chosen for the PANDA solenoid.

D. Coil structural layouts

The general structural layout of the PANDA solenoid coil is shown in Fig. 14. The design of this coil is of the coreless type. It consists of two subcoils. These subcoils are wound by the rectangular conductor with tension of 30 MPa on the Al alloy tubes 15 mm thick. The subcoils are separated with an aluminium spacer. This spacer takes up the axial magnetic pressure of the coils and transmits the reaction from axial ties
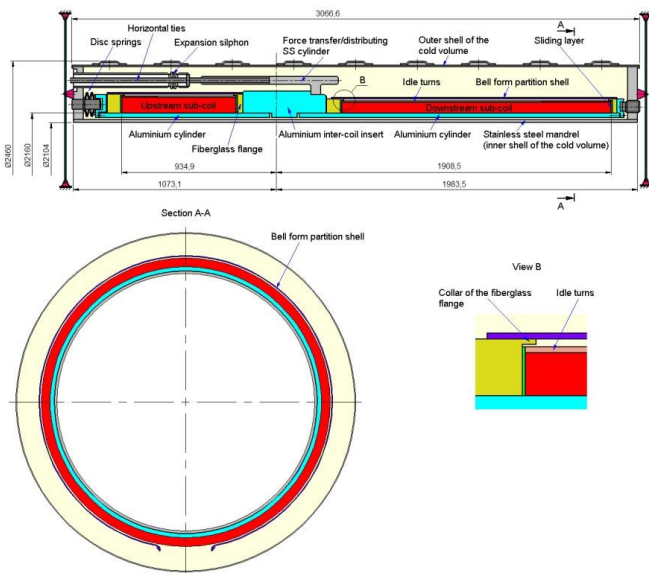
Fig. 14. Coreless coil general structural layout

to the coils.

The Al tube is considered as a secondary dump turn for quench protection of the coil as well.

The subcoils are separating from the aluminum mandrel after cooling down due to thermal contraction difference of the materials (a dominant component of the coil composite is copper). To prevent gluing of the coil surface to the Al tube, a release coating is applied at the tube surface before winding. The separation of subcoils from the tubes provides the natural shape of the coil when the solenoid is energized to avoid touching of the coil and mandrel surfaces in the process of energizing. The friction losses between these surfaces could

be a main source of a premature quench of the coil.

An initial axial precompression of 390 kN is applied to the coil face surfaces. It is done to prevent separation at the contact surfaces coil-insert and coil-flanges under the action of gravity when the coil is cooled. The disc springs 70 mm in diameter on upstream end of the coil united in 60 sets and distributed along the coil flange circle, are used for it. The aluminium and fiberglass flanges are applied to distribute the pressure. The relative axial displacement of a subcoil end with respect to the cold volume shell due to cool down, is of about 3.6 mm. An additional axial subcoil displacement of 0.1 mm is evoked by electromagnetic forces. Changes of the coil length are compensated by the disc spring travel. The prestress is made with respect to the inner shell of the cryostat cold volume.

The friction between the side surfaces of the coils and flanges is not enough to keep the mutual radial allocation of the subcoils and aluminium tubes and to prevent shifting, caused by different thermal contractions. Nevertheless, after cooling down the subcoils remain centered with respect to the aluminium tube due to collars of fiberglass flanges (see Fig. 14).

The fiberglass flanges and the coil face surfaces are separated by PTFE and kapton film layers for decreasing friction motion under the cooling down and energizing.

Coil turn-to-turn insulation – kapton type plus one layer of half lapped prepreg tape (0.12/0.1 mm before and after squeeze). A prepreg interlayer cloth is deposited between the coil layers while winding. In accordance with computations for the conductor rounding 0.3 mm the epoxy content in the prepreg is quite sufficient to fill all interconductor empties in the coil. The corrective coils 3 and 4 are wound above the main coils 1 and 2, respectively. To support the turns of the corrective coils in the axial direction, the idle turns are wound over the main coils 1 and 2.

A heating procedure is applied for the coil to cure the epoxy after winding.

E. Mechanical analysis of the Solenoid Coil

Design models for the mechanical computations

The PANDA solenoid is a complex device, subjected to the loads of three types: ponderomotive, gravitational and temperature loads.

The main problem of the PANDA solenoid design is separation of the superconducting coil on two parts and mechanical stresses on their interfaces resulting from this separation.

The stress strain calculations of the coil composite material were performed by using a computer code COSMOS [12] in the framework of the linear Finite-Element (FE) axially symmetric model of the coil. The electromagnetic loads were applied as nodal forces obtained by the special procedure from the corresponding local flux densities calculated with TOSCA. The temperature loads were applied to the design model of the coil as a uniform temperature field defined in the nodes of FE mesh. Taking into account sliding with friction and appearance of gaps between the coil composite material and

fiberglass flanges, special GAP-elements (contact elements) are included into the model at the coil end faces (only compressive forces can be in these elements).

In the framework of the FE model for thin shells we have analyzed the local concentrations of stresses in the vicinity of the orifice for the target and point application of the axial forces to the intercoil spacer, see the 3D design model of the coil in Fig. 15.
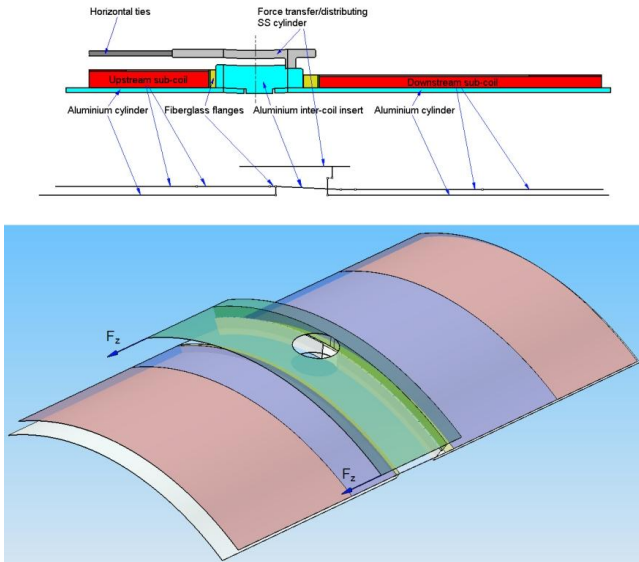

Fig. 15. 3D design model of the coil

The FE model of the outer cryostat shell is shown in Fig.16. The operating loads are: external pressure, point loads of cold mass weight, EMC weight. The EMC weight was considered as distributed over the inner cryostat shell or over two suspending rings.

The value of 0.18 for the friction factor between sliding PTFE and kapton film layers was accepted for computations.
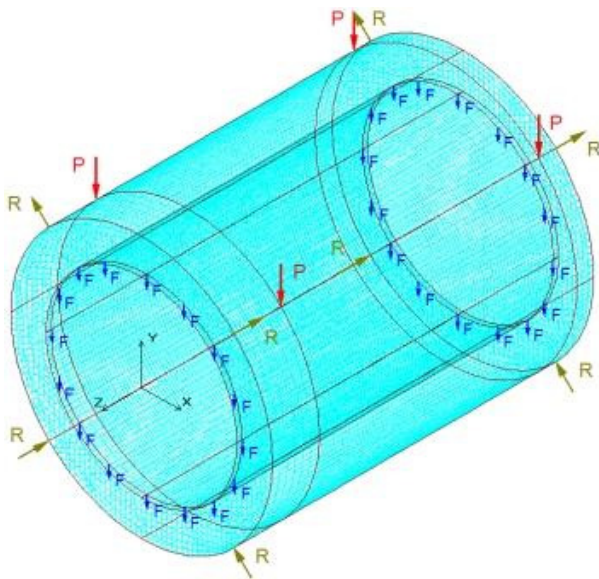
Fig. 16. FE model of the cryostat shell

Design criteria

All constituent parts of the solenoid are checked against the Russian safety code – "Safety requirements of strength analysis of the equipment and pipe lines of nuclear power plants" [13].

In conformity with the accepted standards for detector windings, the maximal value of shear stress has to be about 10 % of the strength limit for shear of a glue epoxy connection at the liquid helium temperature. The shear strength of the epoxy compound at the cryogenic temperature is about 20 MPa. According to [10] the value of shear stress at the coil interface surface 15-20 MPa results in a premature quench of the coil.

We consider acceptable levels of stresses for the coil materials as follows:

- tensile stress for copper $[\sigma]$= 100 MPa,
- tensile stress for insulation $[\sigma]$= 3 MPa,
- compressive stress for insulation $[\sigma]$= 40 MPa,
- shear stress for insulation $[\tau]$= 2 MPa.

The hoop stress in the coil

The hoop stress inside the coil is completely carried by the cable, unlike the detector coils with the aluminium stabilized conductor.

The maximal distributed hoop stress in the coil composite material is 65 MPa. This corresponds to the maximal hoop stress in the copper of the channel <100 MPa. It is an acceptable level for a copper conductor at the liquid helium temperature.

Axial stress in the coil

Maximal axial stresses in the coils 1 and 2 due to the axial electromagnetic forces, calculated within the axially symmetric model, are 28 MPa and 27 MPa, respectively. These values of compressive stresses are acceptable for the coil composite material.

The stresses at the coil sliding surfaces

The results of stresses computations at the sliding face surfaces of the coils 1 and 2 are presented in Table V.

TABLE V
RESULTS OF STRESSES COMPUTATIONS (IN MPa)

Coil 1 left end	σ_Z min / σ_Z max	-2.1/-0.26
	σ_R max	-0.062
	$\lvert\tau_{RZ}\rvert$ max	0.27
Coil 1 right end	σ_Z min / σ_Z max	-19 / -8.5
	σ_R max	1.5
	σ_θ max	52
	$\lvert\tau_{RZ}\rvert$ max	2.1
Coil 2 left end	σ_Z min / σ_Z max	-21 / -10
	σ_R max	2.8
	σ_θ max	36
	$\lvert\tau_{RZ}\rvert$ max	2.1
Coil 2 right end	σ_Z min / σ_Z max	-2.4/-1.1
	σ_R max	0.27
	$\lvert\tau_{RZ}\rvert$ max	0.28

The maximal value of the shear stress in this area is about 2.1 MPa. This value is determined by hoop yielding of the intercoil spacer and its flexibility in the RZ plane. The radial distribution of the shear stress at the left (upstream) face surface of the downstream subcoil (coil 2) is presented in Fig. 17. Owing to optimization of the shape and dimensions of the intercoil spacer and its flexibility in the RZ plane, the separation and misalignment of the sliding face surfaces of the coils and flanges do not appear in the process of cooling
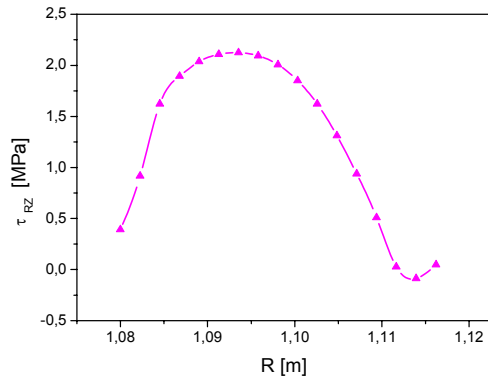
Fig. 17. Maximum shear stress at the upstream face surface of coil 2 as a function of radius

down.

Since the friction factor at the cryogenic temperatures is not a stable value, we have studied its influence on the shear stresses at the coil face surfaces. The maximal value of the shear stress in this area is growing up from 1.6 MPa to 2.2 MPa for the friction factor of 0.1 – 0.25.

Concentrations of stresses near the orifice

In accordance with the results of computations for the thin-walled design model, the local concentrations of axial stresses (membrane) amount to 18 MPa (see Fig.18). The maximal value of shear stress in the winding should be increased by 20% in comparison with the results of the axially symmetric model. So, the maximal shear stress at the coil sliding surfaces
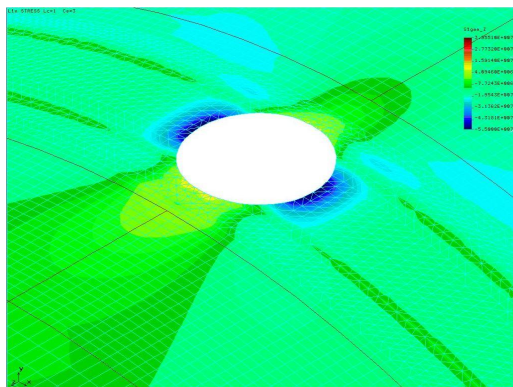
Fig. 18. Distribution of axial stress (membrane) near the target orifice

will be about 2.5 MPa.

Thermal contraction of the coil

The upstream and downstream subcoils become shorter after all loads (spring preload, cooling down and magnetic load) by 4.5 mm and 8.8 mm, respectively. The coil total length (subcoils plus insert) changes from 2841 mm to 2828 mm.

The changes of the coil sizes affect the coil parameters. The force applied to the coils 1 and 3 (see Fig. 3) for the initial dimensions, is 3600 kN and for the corrected dimensions – 3634 kN. The unbalance force applied to the coil for the initial sizes and for the sizes after contractions is 121 kN/105 kN, respectively. It appears that the most serious changes correspond to the integral of radial component of the magnetic field. After cooling down the integral normalized value

TABLE VI
CHANGES OF THE SOLENOID PARAMETERS AFTER COOLING DOWN AND
AFTER APPLICATION OF ALL MECHANICAL LOADS

	Undeformed coil	After cooling down and application of all loads
J, (MA/m^2)	62	62.57
Int (Br)	1.9	2.15
B$_{0.0}$, (T)	2.007	2.018
F$_{Z 1,3}$ (kN)	3600	3634
F$_{Z 2,4}$ (kN)	- 3479	-3529
F$_{Z total}$ (kN)	121	105

changes from 1.9 mm up to 2.15 mm. The changes of the solenoid parameters are listed in Table VI.

It means that the dimensions of the coil have to be initially corrected to keep the optimised parameters after cooling down.

Stress at the interface surfaces with corrective coils

The corrective coils 3 and 4 are wound above the main coils 1 and 2. Essential shear stresses at their interface surfaces (up to 8 MPa) are expected. The reason of it is that the face surfaces of the corrective coils are not supported in the axial direction.

To decrease the value of shear stresses at the interface surface of coil 2 and two-layer correcting coil 4 (see circled area in Fig. 3b), an additional number of idle turns will be

TABLE VII
MECHANICAL STRESSES AT THE CORRECTIVE COIL INTERFACES

Coils 1-3 interface	σ$_Z$ min / σ$_Z$ max	-18 / -1.9
	σ$_R$ max	0.31
	|τ$_{RZ}$| max	0.2
	σ$_θ$ max	68
Coils 2-4 interface	σ$_Z$ min / σ$_Z$ max	-23 / -1.2
	σ$_R$ max	0.28
	|τ$_{RZ}$| max	0.3
	σ$_θ$ max	67

used. These turns providing axial support for the corrective coil turns, will decrease shear stresses at the interface surfaces (see Table VII).

Evaluation of radial gap between the coil and the aluminium tube

After cooling down the clearance between the coil inner surface and the Al tube will appear. The coil obtains a barrel form in the energizing process. The radial deformation of the coil 2 and the aluminium tube after cooling down and application of the electromagnetic loads, are shown in Fig. 19.
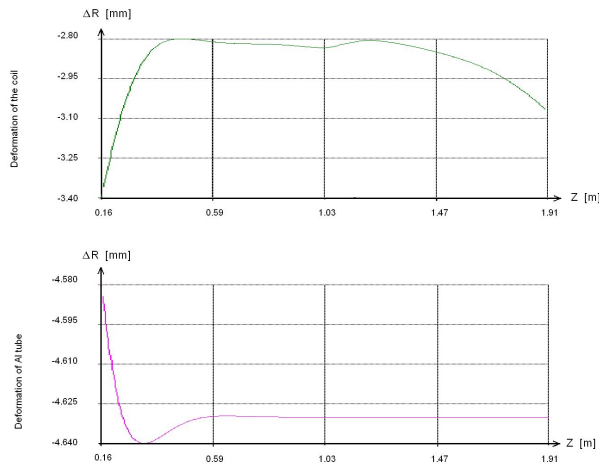
Fig. 19. Radial deformation of the coil 2 and the aluminium tube.

The changes of the clearance between the coil inner surface and the outer surface of the Al tube after cooling down and energizing are shown in Fig. 20. It can be seen that the minimal radial gap after cooling down reaches 0.72 mm and after energizing – 0.91 mm. This gap is quite sufficient to guarantee the absence of mechanical interactions between the coil and the Al tube in the process of coil excitation.
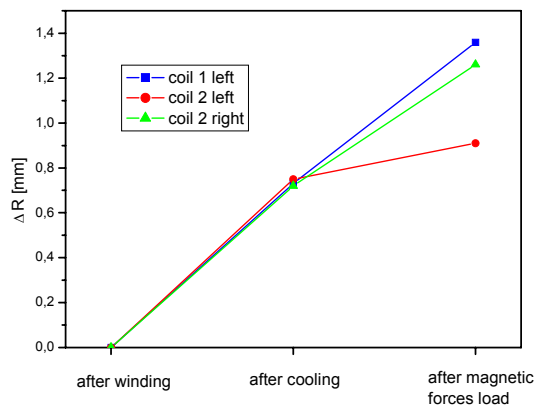

Fig. 20. The changes of the clearance between the coil inner surface and the outer surface of Al tube after cooling down and after energizing

The strength of the outer cryostat shell

Operating stresses in the outer cryostat shell under action of the external pressure, the point loads and the EMC weight calculated in the framework of the design model (Fig.16) are shown in Fig.21. The maximal value of equivalent stress is σ=38 MPa. That is below the allowable stress value $[\sigma]$ = 140 MPa. The maximal value of the outer cryostat shell deformation is about 1 mm, the deformation of the inner shell is less than 0.2 mm.

As it follows from the performed computations, the operation stresses in the coil and in the cryostat shells don't exceed the allowable stresses.

F. Protection System

A quench protection system is based on extracting energy from the series-connected subcoils (Ls) to an external dump resistor (Rd=0.25 Ohm) and to quench protection secondary

dump turn (the Al supporting cylinder) (L_c, R_c) (see Fig. 22). When a quench is detected by the control system of the protection circuit, the protective breakers $(S_1$ and $S_2)$ are opened to a fast discharge in the circuit made up by the solenoid, the dump resistor and the aluminium support cylinder.
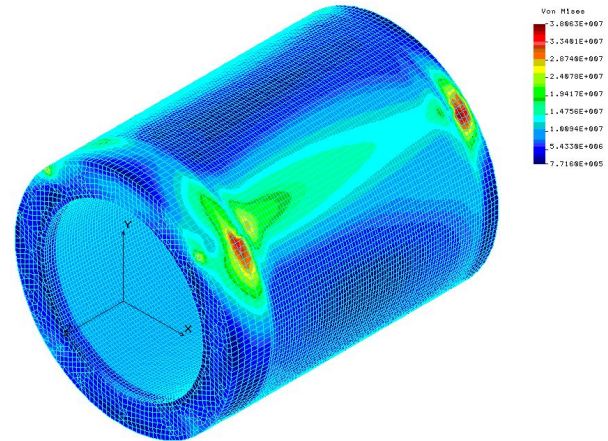
Fig. 21. Von Mises stresses in the cryostat vacuum shell

The electrical resistance of the dump resistor must reduce the maximum voltage on solenoid leads to 500 V.

According to the calculations, the hot spot temperature in the coil after the quench is ~73 K, the temperature of the Al cylinder is ~65 K. The energy accumulated in the coil is partly extracted to the external resistor (24 %) and to the aluminum cylinder (36 %). If the aluminum tube thickness is 10 mm (instead of 15 mm) the energy extracted from the cryostat increases up to 43% and the temperature of the hot spot increases up to 83 K.
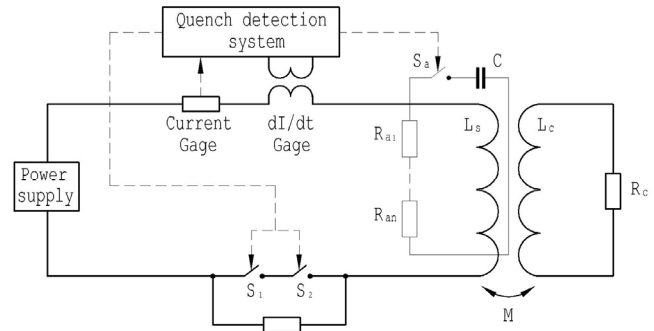
Fig. 22. The coil protection circuit

A failure in the protection control circuit results in maximal temperature rise of the hot spot up to 94 K. This rise is not important for the coreless NbTi coil because it doesn't enclose glue connections with dissimilar materials.

As an additional backup, the active heaters placed on the outer surface of the coil provide a quench back in the whole solenoid coil and thereby limit the temperature gradients inside the coil composite material.

G. Thermal Design

Bath cooling was chosen to obtain the assured thermal stabilization of the conductor. This type of cooling allows to use cryocoolers for recondensing of helium, refilling helium

from Dewar vessels or to use circulating method of cooling. That implies the coil to be placed in the closed helium volume of 1.8 m^3. This volume is contained in the vacuum chamber and supported by high thermal resistance ties and struts. The cold volume is surrounded by the thermal shield supported from the side of the vacuum chamber and cooled by liquid Nitrogen.

Thermal shield

The layers of aluminized mylar are applied to reduce heat load on the thermal shield. The data of the thermal load at the thermal shield multiplied by the safety factor 2, are presented in Table VIII. An additional thermal load given by eddy currents in the cryostat shells occurs when the coil is ramping up or discharging. A time interval for energizing the coil which ensures an acceptable heat load, is about 1 hour. The overall heat load at the level 77 K is expected not to exceed 346 W in the operational mode and about 351 W while

TABLE VIII
HEAT LOADS ON THE COLD VOLUME AND ON THERMAL SHIELD

T=4.2 K	Load, Watt
Radiation	0.44
Support and chimney conduction	1.8
Residual gas conduction	0.16
Conductor joints and wires	0.7
Eddy current losses in the Al cylinder	16
Current leads	0.64
Total (normal/transit regime):	**3.8/21.8**
T=77 K	
Radiation	130
Shield supports	30
Heat intercepts of the coil supports	144
Eddy currents	5
Current leads	42
Total (normal/transit regime):	**346/351**

ramping.

Cold mass support

Four low-heat-conduction vertical ties, 6 axial ties and 16 radial struts support the cold mass of the cryostat. The integral thermal conductivity of the stainless steel supports was accepted to be 0.04 W·m/cm^2 in the interval 77 K – 4.2 K and 0.27 W·m/cm^2 – in the interval 300 K – 77 K.

Helium vessel

A radiation load of 0.22 W has been estimated for the cold volume. This value is obtained for 43.8 m^2 of the cold volume surface covered with stainless steel foil of 50 μm sputtered by high purity aluminum to reduce radiation heat loads [14, 15]. The treated surfaces are characterized by the following:
- Reduction of gas extraction by factor 10^4;
- Exclusively low emissivity: < 0.005 at 4.2 K.

The new process of surface treatment includes evaporation of Al on a substrate heated up to 300-400ºC in a flow of pure gaseous helium. Residual gas conduction for the temperature interval of 77 K-4.2 K and vacuum 10^{-7} torr is 0.00181 W/m^2.

The data of the heat load at the level of 4.2 K multiplied by the safety factor 2, are summarized in Table VIII. The thermal load due to the eddy currents in the aluminum shells is presented there as well. The overall heat load at the level of 4.2 K is expected not to exceed 3.8 W in the operational mode and about 21.8 W - in the transient mode.

If for some reasons the stainless steel foil sputtered by high purity aluminum is not acceptable for the solenoid design, the cold volume surface and inner surface of the thermal screen can be covered with high purity aluminum foil. The radiation load on the cold volume will increase by an order of magnitude at that.

HTS current leads

It is planned to use HTS current leads [16]. They are designed to conduct cooling and do not require helium flow cooling. Its conductive heat leak is only 0.64 W at 77 K – 4.2 K per pair and the current of 2050 A (Table VIII).

The "warm" parts of the current leads (77 K – 300 K) cooled by liquid Nitrogen are optimized to provide minimum energy consumption at the level of 77 K. The current leads are located in the bottom part of the cryostat to secure cooling by liquid Nitrogen in case of a cryocooler emergency.

The data of the current leads heat load at the temperature levels of 4.2 K and 77 K, are presented in Table VIII.

Heat losses in conductor joints and wires

The conductor electrical joints of the coil are made by soldering. The electrical resistance of each joint is better than 10^{-8} Ohm (power dissipation is less than 4 10^{-3} W).

A resistive drop at the end cap of HTS current leads accepted by liquid helium, is ~24 mW per lead. The warm end (77 K) resistive drop accepted by liquid Nitrogen, is 0.7 W per lead [17].

H. Control, Diagnostics and Instrumentation

The measurements should be used to control the normal operation of the solenoid and generate alarm and interlock signals for a magnet safety. The diagnostics includes the following systems:

Quench detection. The resistive zone must be detected to protect the solenoid when a quench. An electronic system, insensitive to spurious signals and interferences, and protected against the voltage development across the coil, will be used.

Voltage taps. The potential drop of the current leads at the both sections (Cu and HTS), the electrical resistance of the coil in the process of cooling down and the conductor joint resistance, will be monitored by means of voltage taps.

Temperature control. The temperature of the solenoid coil and its mandrel is controlled with several thermo-resistors. The thermal shield temperature is controlled with linear temperature sensors.

Stresses and forces control. Strain gauges are mounted on the coil outer surface to control the stress levels during the solenoid energization. Six further strain gauges are mounted on the tie rods which counteract the axial magnetic force due to the magnetic system asymmetry.

Vacuum pressure control. Two pressure gauges control the normal operation of the vacuum system. The pressure signals are also used as an interlock to discharge the solenoid after a vacuum failure.

Since the access to the sensors mounted in the cryostat would require a major disassembly, all the transducers are

duplicated with independent wiring to increase the reliability.

I. Design of the cryostat

Vacuum vessel

Stainless steel was chosen as the material of the vacuum vessel of the cryostat to ensure its mechanical stability. The ends of the shells are thickened to provide means for anchoring the rods supporting the coil (Fig. 3). Wall thickness of the inner shell of the vacuum vessel is 12 mm. The electromagnetic Calorimeter of about 170 kN is fixed on this shell. The outer shell of the vacuum vessel has 8 stiffening ribs of 24 mm x 38 mm (in radial and axial directions, respectively). At the top of the upstream part of the outer shell there is a flanged branch where both cryocoolers, the chimney for liquid and gaseous N_2, LHe and GHe inlets and outlets, are mounted. The diagnostic wires connectors, relief valves and flanges for vacuum pumping are located on this flange as well. The weight of the vacuum vessel is 5.5 tons.

Cold volume vessel

The cylindrical shells of the cold volume are produced from stainless steel. The wall thicknesses of the cold volume shells are 10 mm for the inner wall and 4 mm – for the outer wall. The inner shell of the cold volume takes the axial prestress 390 kN of the disc springs after the coil assembly before cooling down. Besides, the inner shell transfers the weight load to the cold mass supports.

Cold mass supports

The forces acting on the solenoid cold mass are its own weight (99 kN) and the axial magnetic force (121 kN). A sufficiently high axial offset force is required due to the unidirectional action of axial ties and a considerable axial force gradient (91 kN/cm). The coil suspension system consists of twenty stainless steel supports (03Cr20Ni16NMn6) fixed at the ends of the outer vacuum shell. 4 vertical rods take the weight of the cold mass and 16 radial ties center the cold mass vessel with respect to the outer vacuum shell. The axial magnetic force is carried by six stainless steel rods (Fig. 3a). The position of the coil has to be adjusted taking into account thermal shrinkage of the coil and its supports as well as the yielding of the support ties. An axial shift of the coil of ±10 mm causes the axial force of ±91 kN that sets up strict requirements on the coil adjustment precision.

The coil package (two coils, flanges, intercoil insert) is prestressed by disc springs. The friction at the face surfaces of the coils and the surfaces of the flanges prevents sliding coil down and fix the coil in space. The gravity load is transmitted from the coil to the suspension system via flanges of the coil supports and end caps of the cold volume.

In axial direction the magnetic force load is transmitted from the coils to the low-thermal conducting axial tie rods via the aluminum intercoil insert, pressed by two coil parts, then – via a stainless steel distributing ring. The aim of this ring is equalization of the non-uniformity of the axial stress at the coil side walls due to localized load of the axial ties.

Bell form partition shell

The bell form partition shell is mounted around the solenoid coil in the cold volume. This shell has to prevent boiling up of all liquid helium in the cryostat after a quench. In the process of cooling down the cold gaseous helium is flowing over the surface of the coil. The levels of liquid helium inside and outside the partition are equal after the cryostat is filled up with liquid. In case of a quench the liquid helium is boiling up at the surface of the coil inside the partition shell. The vapor prevents additional liquid helium entry into the partition space and thus the further evaporation process is retarding.

Thermal shield

The thermal shield of the cryostat is made of copper. A stainless steel circular vessel for liquid Nitrogen is located at the upstream part of the thermal shield. The shield is fixed with respect to the outer vacuum shell by means of fiberglass spacers. The cold head of the cryocooler is connected to the wall of the vessel for liquid Nitrogen via flexible copper foil. The weight of the thermal shield and liquid nitrogen vessel is 1.5 tons.

Current leads

The current leads are located in the bottom part of the cryostat to provide the secured cooling in case of emergency stoppage of the cryocooler. The layout of the current leads in the bottom part of the cryostat is shown in Fig. 23. The HTS parts of the current leads are located in the gap between the cold vessel and thermal shield in angular direction. Metallized ceramics is applied for wall tube insulators to provide vacuum tightness. The warm copper parts of the current leads pass through the liquid nitrogen vessel via axial tubes welded in its
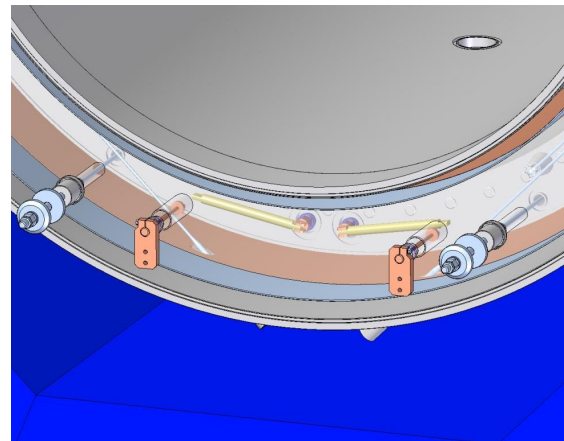

Fig. 23. The current leads layout

walls.

The "warm" ends of the current leads will be ventilated with a fan to prevent moistening.

The general weight of the cryostat equipped with the coil, is 17 tons (without cryocoolers).

J. Iron Yoke

Barrel and end caps design

The iron yoke is intended to return the solenoid magnetic flux. Besides that, the contribution of the yoke to the total magnetic field in the tracker area is about 12 %.

The yoke has an octagonal shape. It is closed with unequal end caps on the both sides (see Fig. 3a). The distance between the outer radius of the cryostat and the inner surface of the

yoke makes up 214 mm for placing muon detector panels on inner surface of the barrel part, for simplification of the assembly procedure and for cabling.

The upstream end cap has a central round hole and the downstream end cap - the rectangular one. The end caps are separated into two parts. The downstream end cap can be opened. It is mounted on the skids. The main components of the return yoke, their marking and weights are shown in Fig. 24. The end caps in the process of the magnet operation are exposed to the action of its own weight (upstream door weight is 2x16.6 ton, downstream door inner part weight is 2x10.5 ton, outer part – 2x7.9 ton) and magnetic pressure (the force applied to the upstream door is +1422 kN, the force to the downstream door is –1540 kN).

The rectangular radial passages between doors and barrel parts are created for tubes and cables servicing various detectors.

The total weight of the yoke is 250 tons. The yoke is built of modules bolted together. Since the crane capacity in the hall assembly area is limited by 15 tons, every block of the octagonal modules is separated in two pieces. The maximal weight of these pieces doesn't exceed 12.2 kN. The material of the modules is low carbon steel (Steel 10).

Muon detector system

Apart from returning the magnetic flux the iron yoke will be used for muon detection. The iron beams of the yoke barrel and end caps will be split to house the muon detectors chambers.

The cryostat must be sufficiently transparent for muon detection. Average nuclear interaction length of the cryostat within the angular domain 25÷140 deg. is $L/\lambda_{int} = 0.6$.

At the moment the final decision has not been made concerning the number of layers of muon chambers.

Shielding box and trim coils for the DIRC

The steel shielding box for the DIRC jointly with the trim coils c1 and c2 are intended to decrease the stray fields in the area of photomultiplier tubes up to the acceptable value of 1 mT. The shielding box (see Fig. 24) is assembled of several separate modules and has the same octagonal shape. It is fixed
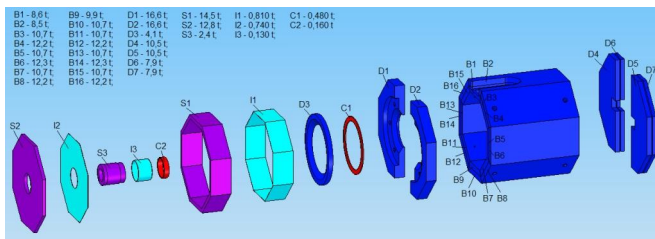
Fig. 24. The components of the return yoke and shielding box, their marking and weights

at the upstream cap of the yoke. The main parameters of the shielding box are listed in Table IX. The total weight of the shielding case is 32 tons. It is made of low carbon steel (Steel 10). Pure iron sheets 10 mm thick are distributed on the inner walls of the shielding box to additionally improve its screening capability.

Two trim coils c1 and c2 made of the hollow copper

conductor, are placed at the inner tube of the shielding box and embedded in the upstream end cap of the yoke to ensure the low level of stray fields in the area of PMT's. The coils are cooled with demineralized water. The coils are vacuum

TABLE IX
PARAMETERS OF THE TRIM COILS AND SHIELDING BOX

Trim coil average current density	3.8 A/mm^2
Losses in the trim coils	29.4 kW
Weight of steel in the shielding box	30000 kg
Weight of Pure Iron	1700 kg
Weight of Copper in the trim coils	440 kg

impregnated with epoxy rezin.

Space frame

To ensure the stability of the iron yoke and reproducibility of its sizes, an outside space frame is applied. It is welded from I-form beams.

Assembly of the solenoid

The first assembly of the return yoke will be done by the producer at his place.

Assembly of the return yoke in the PANDA hall will be done on the transportation carriage in the assemble area. The carriage and the solenoid space frame are mounted on temporary supports to provide stability of the construction.

Initially seven of eight bilayer modules will be assembled (see Fig. 25). Before mounting the upper beam, the cryostat has to be inserted into the yoke barrel and placed on a temporary support. After mounting the barrel top beam and top framing beams, the cryostat is suspended on radial supports. The upstream yoke door is rigidly fixed on the barrel. The downstream door will be mounted on the skids to provide its opening (see Fig. 26).
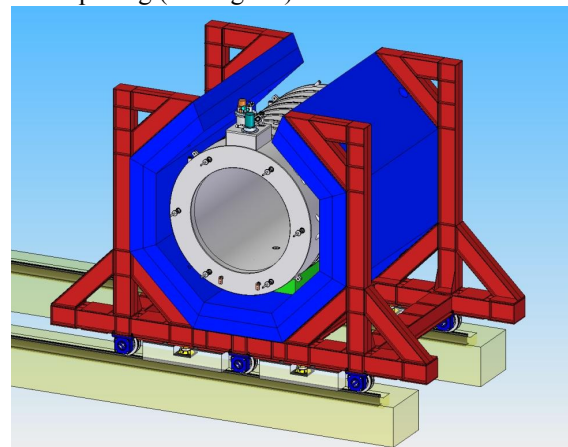

Fig. 25. Assembly of the return yoke

Before transportation of the assembled yoke the temporary supports will be removed by means of jacking. The DIRC shield box and trim coils will be mounted after fixing the yoke in its operation position.

Adjustment of the solenoid to the beam line

The central line of the coil has to be adjusted with respect to the return yoke central line within precision of 10 mm by means of the radial support length correction.
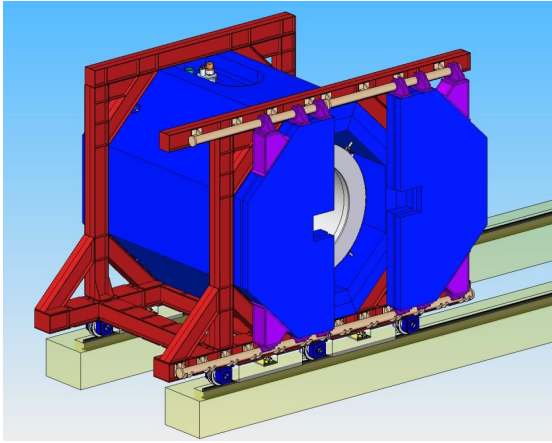
Fig. 26. Sliding downstream doors

The axial position of the coil has to be adjusted within ±10 mm by the length corrections of axial ties.

Finally the assembled solenoid has to be adjusted to the beam line. It will be done by means of adjusting shims under the solenoid footprint.

IV. CRYOGENIC AND VACUUM SYSTEMS

Cryogenic System

The method of the solenoid cooling is initial fillup of the cryostat vessels from dewars with liquid Helium and liquid Nitrogen and subsequent re-condensing of liquids by 600 W Cryotech Nitrogen cryocooler [16] and 4.2 W Sumitomo three stage helium cryocooler [17] (see Fig. 27).

The use of cryocoolers allows to achieve the complete
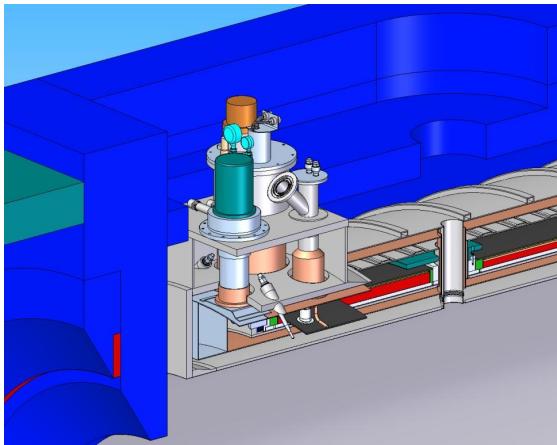
Fig. 27. Allocation of the cryocoolers and branch pipe for helium tubes

independence from a local helium supplier. At the same time in emergency situations with cryocoolers, the cryogenic liquids from the local supplier can be used for period of maintenance without shutdown of the detector.

If the stainless steel foil sputtered with high purity aluminum is not applied and the cold volume surface and inner surface of the thermal screen are covered with high purity aluminum foil, an additional cryocooler has to be used

to compensate the increased radiation load on the cold volume.

Liquid Helium is necessary to provide operation conditions of the superconducting coil when the cryocooler is not switched on, and to maintain efficient heat exchange between the cryocooler cold head and solenoid surface.

Liquid Nitrogen is necessary to run the thermal shield, to provide operation conditions of the shield when the cryocooler is not switched on, and to fix the temperature at the "warm" parts of HTS current leads.

In case of emergency shutdown of a cryocooler or in case of its service, the system must survive a definite period of time (48 hours, at least) to resume the cryocooler operation or to refill the tanks with liquid nitrogen and helium.

Very fast overheating of the superconducting winding and evaporation of all the helium contained in the magnet, takes place in case of the magnet "quench". In this situation a thermal status requires partial re-cooling of the solenoid coil, refueling liquid helium and total re-energization.
Modern cryocoolers need regular scheduled maintenance at 10000 hour intervals.

Vacuum System

After installation of the solenoid in the cryostat it will be cooled to LN_2 temperature and leak tested.

The pumping system consists of a forepump and a turbo-molecular pump to ensure an ultimate pressure of $\sim 10^{-5}$ torr (at room temperature). The pressure drop up to $\sim 10^{-7}$ torr has to be reached by means of cryo-pumping of the vapors onto the cryogetter charcoal panels after cooling down.

A relieve valve for an overpressure of 0.2 bar must be provided in the vacuum system to avoid pressure increasing in the cryostat caused by cryo-pumped gases while quick temperature rising.

V. POWER SUPPLY

The power supply should be selected with 1/3 margin against the operation current to be capable of energizing the solenoid to the full current in about 20 minutes. It must operate with stability of ±0.1 %.

The power supply has to be connected to the solenoid current leads by insulated flexible copper cables (maximal current density 1 A/mm^2, maximal length 30 m). The cables should be air cooled.

The circuit breakers and dump resistors are used to protect solenoid against a failure from overheating after a quench. The circuit breaker is made of two independent switches to increase safety redundancy.

The dump resistor has to absorb up to 9.5 MJ with a peak energy rate of about 1 MW. A water cooled stainless steel resistor with a mass of 200 kg is appropriate for this.

VI. QUALITY ASSURANCE AND MANUFACTURING

It is supposed that the iron yoke, the solenoid coil and the cryostat will be produced by the same manufacturer to make him responsible for the final parameters of the magnet system.

The manufacturer of the PANDA solenoid will have to provide a written Quality Assurance Plan or Manual,

generally in accordance with the requirements of ISO 9001. The Plan will describe as a minimum the QA organisation, authorities and responsibilities, requirements for the design and procedural documentation, requirements for control of manufacturing, procurement and inspection operations; requirements for record keeping and audits.

When the return yoke and the cryostat are manufactured, assembled and tested at the producer place, they will be transported to GSI and finally assembled. The acceptance test including field mapping will be performed there.

VII. CONCLUSION

The novel JINR design of a large PANDA detector solenoid has been developed.

The lower requirement to radiation transparency for the PANDA solenoid cryostat allows one making the coil design different from traditional designs of large detector solenoids with aluminium stabilized coils and circulating indirect cooling.

The application of the copper stabilized conductor combined with helium bath cooling and re-condensing of evaporated helium and nitrogen by cryocoolers, would significantly reduce the cost of the PANDA solenoid maintenance.

REFERENCES

[1] J. Ritman. Conceptual Design and Simulation of the PANDA Detector. Preprint to Elsevier Scince. 18 July 2003.

[2] E.K. Koshurnikov, A.A. Efremov, Yu,Yu. Lobanov, A.F. Makarov, H. Orth, A.N. Sissakian, A.S. Vodopianov. Conceptual Design of the PANDA Magnet System. MT-19, *IEEE Transactions on Applied Superconductivity*, vol. 16, N. 2, 2006, p. 469-472.

[3] A. Herve at al., "Status of the Construction of the CMS (Compact Muon Spectrometer) magnet", in Proc. 18th Intern. Conf. on Magnet technology (MT-18), Vol. 14, No 2, 2002, p. 548.

[4] A.B. Oliva et al., "Zeus magnet construction status Report", in Proc. 11th Intern. Conf. on Magnet technology (MT-11), Tskuba, 1989, p.201.

[5] A. Yamamoto et al., "Progress in ATLAS Central Solenoid Magnet", IEEE Trans. On Appl. Superconductivity, vol.10, 2000, p.353.

[6] A. Makida et al., "Development of a Superconducting Solenoid Magnet System for the B-Factory Detector (Belle)", *Adv. In Cryog. Eng.,* 1998, vol. 43: p. 221-228.

[7] OPERA 3D – Software for Electromagnetic Design. TOSCA 9.0 Reference Manual. Vector Fields Ltd., Oxford, UK, 2003.

[8] H. Hillman. Fabrication technology of superconducting materials. Superconductor Materials Science. Ed. by Foner and Shwartz, 1981, Plenum Press, 275-361.

[9] M.Wilson. Superconducting Magnets. Clarendon Press, Oxford, 1983.

[10] E.Bobrov, at al. Experimental and theoretical investigation of mechanical disturbances in epoxy-impregnated superconducting coils. Cryogenics, 1985, Vol.25, June, pp. 307-326.

[11] J.S Alcorn, H.O. Peterson, S.J.St.Lorant "The SLAC Two-Meter Diameter, 25-kilogauss, Superconducting Solenoid" IEEE Pub. N 72CH0682-5TABSC, Applied Superconductivity Conference, 1972, Annapolis, Maryland, pp.273-276.

[12] COSMOS M v 2.95 User's Guide, System Research and Analysis Corp., Los Angeles, 2005.

[13] "Safety requirements of strength analysis of the equipment and pipe lines of nuclear power plants " *RF Regulation* PNAE G-7-002-86

[14] M.Larin Preparation of the thin film coatings allowing ~10^4 reduction in gas emission on the surfaces of ultra-high vacuum system. J.Vac.Sci. Technol. A., ser.2, v13, N5,1995, p.2579-2581

[15] M. Larin, T. Mormose, H. Ishimary, and N. Gotoh, "Liquid helium cryopumps with low-emissivity Al film coating and low helium consumption," *Journal of Vacuum Science and Technology A. Second series*, Vol. 13, Number 5, pp. 2579–2581, Sept./Oct. 1995.

[16] HTS-110 Ltd: "The CryoSaver family of current leads" [Online]. Available: http://www.hts-110.com/products/current-leads.html

[17] Jürgen Kellers. «CryoBloc and CryoSaver. Designing Magnets with HTS Current Leads», American Superconductor information, November, 2003.

Joint Institute for Nuclear Research

2 T Superconducting Detector Solenoid for the PANDA Target Spectrometer
Part 2
Conceptual Design of the Laminated Iron Yoke

Dubna
2007

I. INTRODUCTION

Unlike the iron yoke design presented in part 1 of this report [1], the real design of the yoke has to take proper account of the muon system. Towards this end for better registration of the muons and suppression of background, the iron yoke should be laminated. The optimal lamination of the yoke modules is the following: iron plates of 30-50 mm are interleaved by about 20 mm gaps for positioning of muon detector planes. Such scheme of detector planes distribution provides the possibility of defining the space point where the muon stops. This is the well known "range system" successfully used in a number of experiments [2, 3].

II. DESIGN OF THE LAMINATED IRON YOKE

The yoke consists of the octagonal barrel part and two end caps. The solenoid cross section is shown in Fig. 1. Steel 10 plates of 30 mm thick are interleaved by 20 mm gaps for allocation of muon detector planes. The upstream end cap is not laminated and it bears the weight of the DIRC steel shielding box and trim coils. According to the muon detector group requirement to have an upstream access to the muon system detector connections, the upstream end cap is allocated inside the octagon barrel.
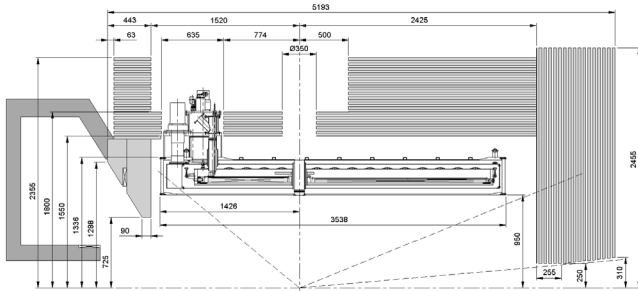
Fig. 1. PANDA solenoid layout, side view.

The downstream door is a sliding one and it is mounted on the skids. To provide the additional rigidity, the yoke is consolidated by means of two outer support frames. The 3D view of the solenoid is shown in Fig. 2.

III. MAGNETIC FIELDS AND FORCES

A. Field homogeneity and balance of forces

The change of the yoke design by applying the split iron beams instead of the solid beams practically does not affect the field homogeneity in the operation area; the maximal value of line integral of the radial field component in the TPC region increases by less than 1 % and later on it can be compensated by the change of parameters of correcting coils placed at the ends of the main coils.

However, due to redistribution of magnetic flux in the iron (Fig.3), the net axial force applied to the coil in case of this modification would be approximately equal to zero

(instead of +121 kN for the solid yoke option). Since the axial tie rods are intended for carrying tensile loads only (not for compressive loads), the uncertainty of the axial load sign is not acceptable from the point of view of mechanical design. The axial force gradient in axial direction is $\Delta Fz/\Delta Z = 91$ kN/cm. Later on special measures should be undertaken to solve this problem.
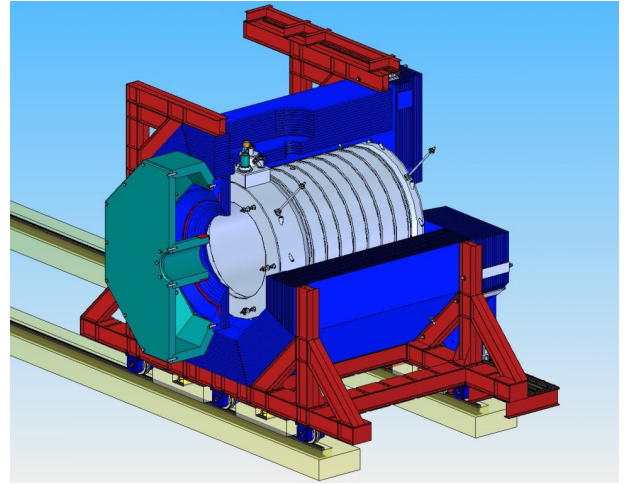

a)
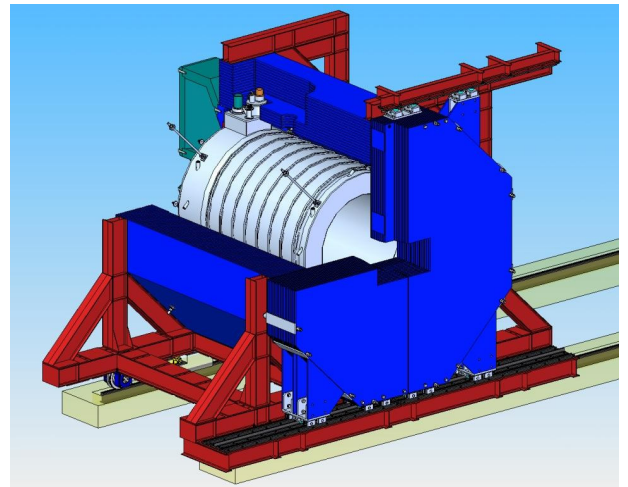
b)

Fig. 2. 3D view of the PANDA solenoid: a) from upstream side, b) from downstream side

B. Stray field in the DIRC PMTs region

In the area of DIRC PMTs on the sphere of radius R=1 m the maximal value of magnetic flux should be limited by 1 mT (Fig.4). The increased up to 1.2 mT value of the flux density in this area can be corrected by the trim coils.

C. Magnetic induction in the iron yoke

Lamination of the yoke beams leads to changes of the flux density and of the forces acting on the iron beam parts. Radial dependence of the flux density for both options (solid and laminated) is shown in Fig. 5. The downstream end cap (Fig. 6) that now consists of 17 iron plates (the first

one of 5 mm and the other of 30 mm thickness) is subjected to action of the axial magnetic force of about 170 ton. The
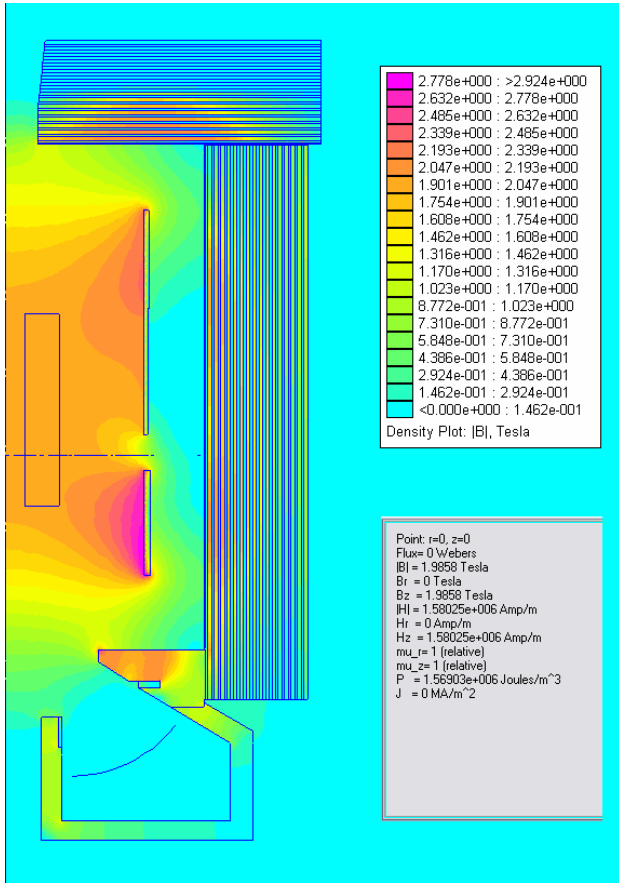

Fig. 3. Magnetic flux density for the laminated iron yoke.

axial dependence of flux density in the downstream end cap is shown in Fig. 7. The forces acting on the first 10 plates are given in Table 1. The high level of forces imposes
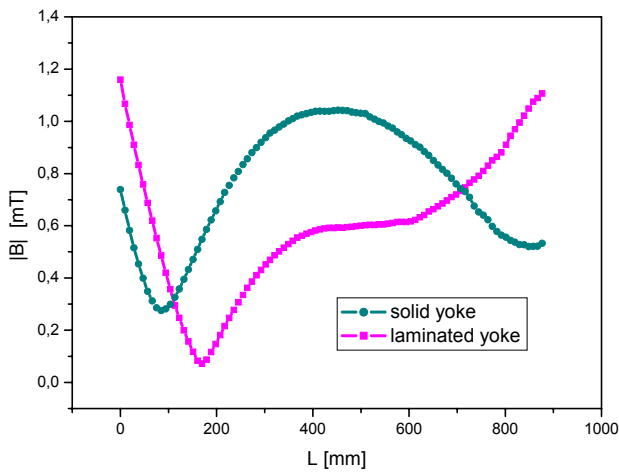

Fig.4 Stray field in the PMT region (R=1m) as a function of distance L along the circular arc.
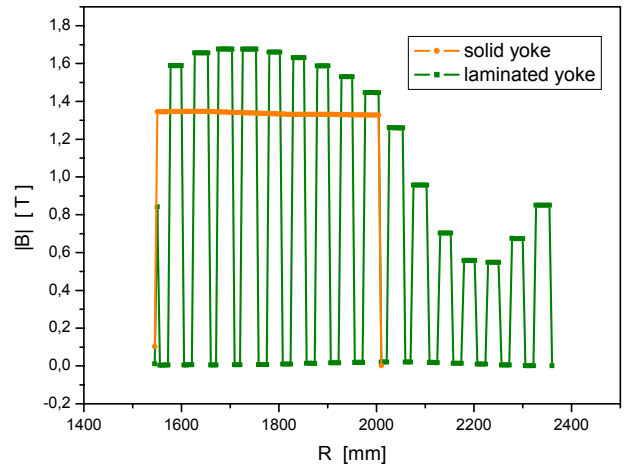
Fig. 5. Flux density in the yoke (Z=260 mm) as a function of radius.

additional requirements on the fixation of the separate plates apart from around the periphery.
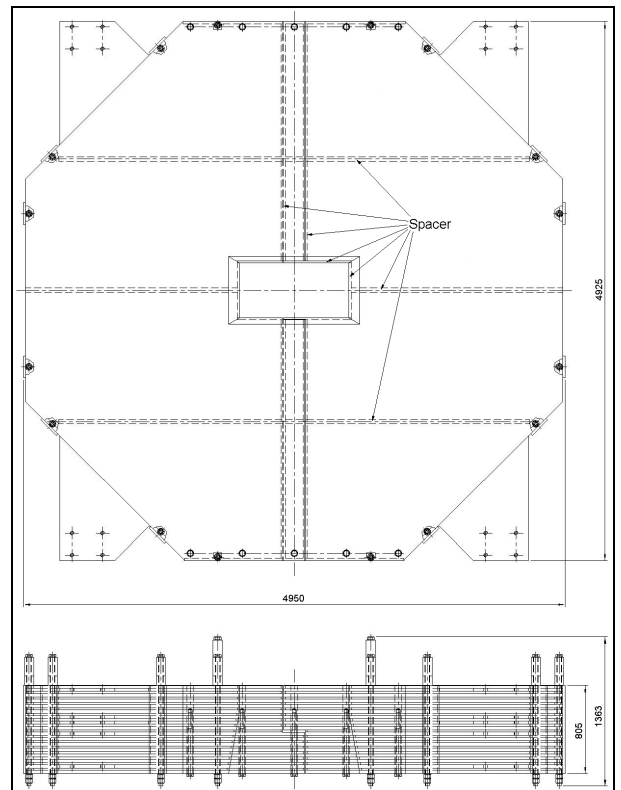
Fig. 6. Downstream end cap of the iron yoke.
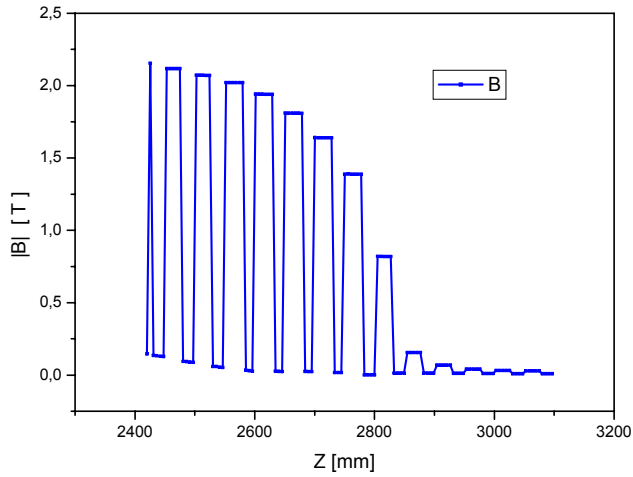
Fig. 7. Flux density in the yoke downstream end cap.

TABLE I

AXIAL FORCES ACTING ON THE IRON PLATES
OF THE DOWNSTREAM END CAP

Plate No.	Fz [kN]
1	-147
2	-483
3	-373
4	-289
5	-214
6	-146
7	-88
8	-41
9	-8.3
10	-0.4
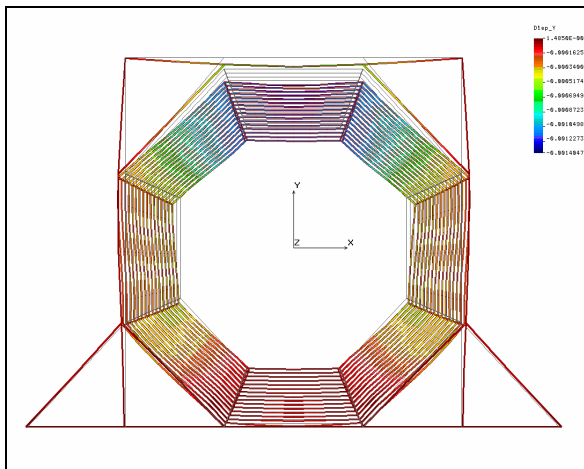
Fig. 8. Deformation of the yoke due to its weight
(large scaled plot).

IV.   DEFORMATIONS AND STRESSES

The mechanical analysis of the return yoke has been done by the finite element method. Deformation of the yoke in its cross section is calculated for two load cases:

a) yoke own weight G = 2100 kN;

b) own weight and horizontal load P_x = 0.25 G (seismic load).

The barrel part of the yoke consists of 8 beams that are bolted together over the edges of the outer octahedral surface. The yoke is supported by two frames. The mechanical properties of the yoke material (Steel 10) are:

$$\sigma_u = 330 \text{ MPa,}$$
$$\sigma_y = 200 \text{ MPa.}$$

The own yoke weight load results in the vertical direction deformation u_y with the maximal value
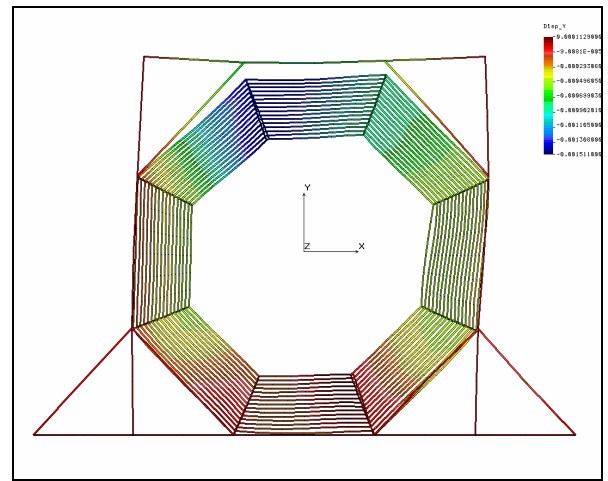
Fig. 9. Deformation of the yoke due to weight and horizontal loads.
(large scaled plot).

u_y = 1.4 mm (Fig. 8).

In case of weight and horizontal loads the maximal vertical and horizontal deformations are u_y = 1.5 mm and u_x = 2.0 mm (see Fig. 9). The frames significantly increase the rigidity of the yoke. Their absence would lead to deformation u_y = 6.5 mm.
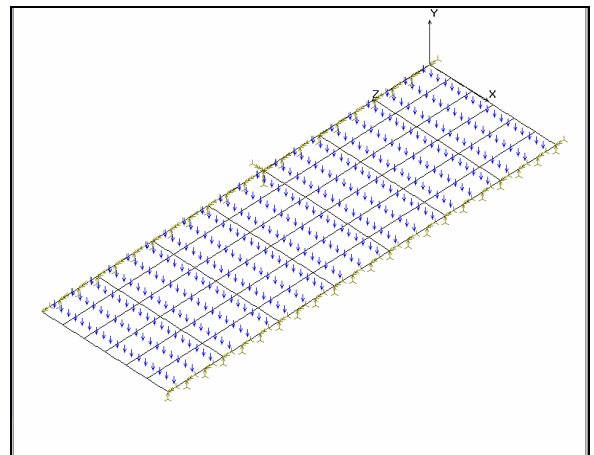

Fig. 10. Model of the inner 30 mm plate of the yoke octagonal barrel.

The maximal stress in the plates due to weight and seismic load is $\sigma_{max} = 14$ MPa, that is essentially lower than the yield point stress of the material.

The results of computations of deformations and stresses due to magnetic forces for the inner yoke plate are shown in Fig. 10-12. The plate is loaded by magnetic pressure, non-uniformly distributed over its surface (see Fig. 10). The magnetic forces were calculated using TOSCA code.
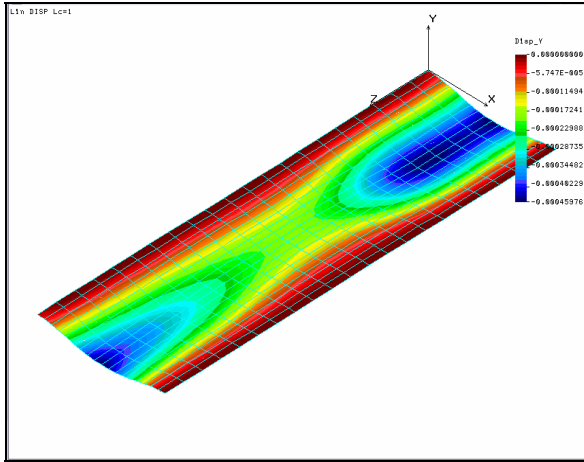

Fig. 11. Bending deformation of the inner plate.

The maximal plate deflection is 0.5 mm (Fig. 11), the maximal stress is $\sigma = 28$ MPa (Fig. 12).
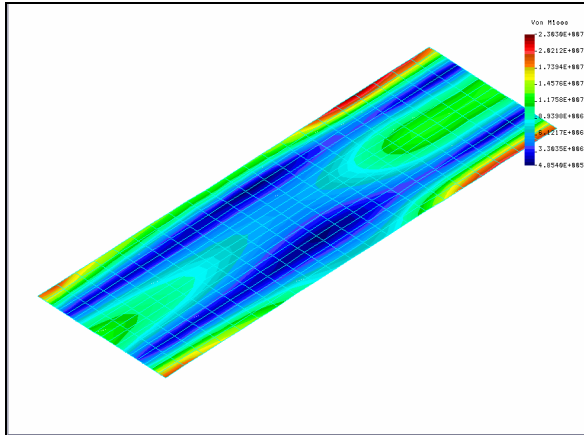
Fig. 12. Von Mises stresses in the inner barrel plate.

The bending deformation of the mostly loaded 30 mm plate in the downstream end cap is 0.7 mm (Fig. 13), the maximal stress in it is $\sigma = 31$ MPa (Fig. 14).

The evaluated stresses and deformations are within the acceptable limits.

V. CONSTRUCTION OF SOLENOID

The cross section of the solenoid with laminated iron yoke is presented in Fig. 15. The yoke barrel beam plates are welded via 20 mm spacers at the outer sides. The beams are consolidated with each other by means of eight bolts at
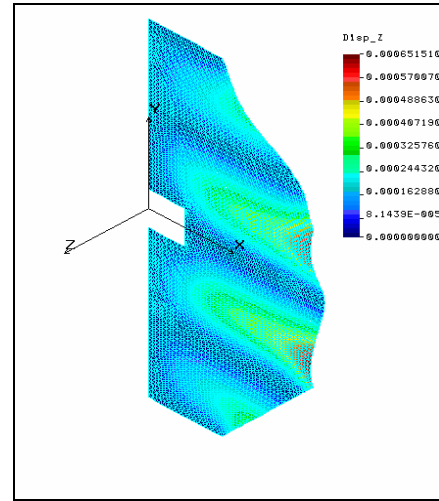

Fig. 13. Deformation of 30 mm plate in the downstream end cap.

every butt of outer plates (Fig. 16). Additionally, interlock connections will be used at the barrel beam interfaces.

The downstream door includes two stacks of metal sheets separated by means of 20 mm thick spacers and welded to each other. The connections of the plates are made at the periphery of the plates. Besides that, to provide horizontal stability of the door, three horizontal sets of welded spacers are applied (Fig. 6).
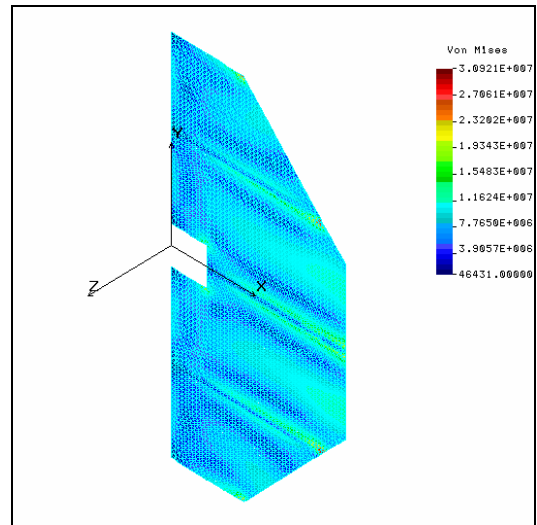

Fig.14. Von Mises stresses in 30 mm thick plate of the downstream end cap.

Similarly to the previous option of the iron yoke [1], to ensure the stability of the yoke and reproducibility of its sizes, an outside space frame is applied. It is welded from I-form beams and fixed by bolts to the outer beam plates.

The upstream end cap is placed inside the barrel part of the yoke and joined with the first 30 mm thick plates of the barrel beams. The downstream door is attached to the outer plates of the barrel beams through the spacers by means of bolts (Fig. 6, Fig. 15). All parts of the yoke including halves of the doors are rigidly fixed to each other to provide general stability of the construction.
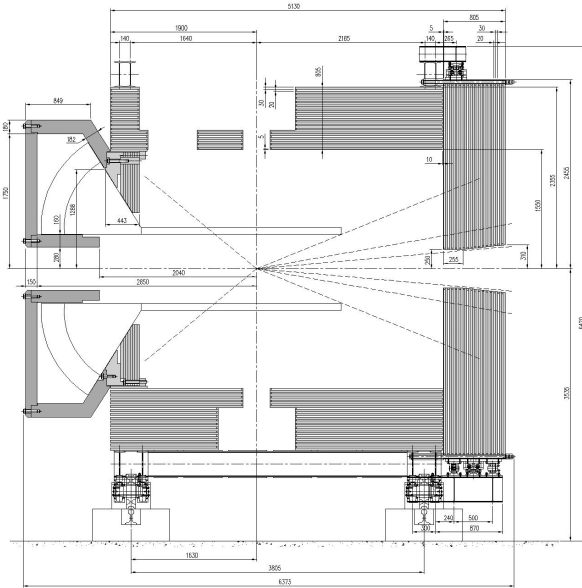
Fig. 15. Cross-section of the solenoid.

In transfer position (transportation of the solenoid from the assembly area to the beam area) the sliding door has to be fixed to the barrel by bolts. In the process of assembly and in operation position, when the door may be opened, there are addition skid supports to bear the weight of the door (Fig. 17). It takes a system of load-bearing wheels and horizontal guiding rollers at the top and at the bottom of the door parts to provide sliding of the door.
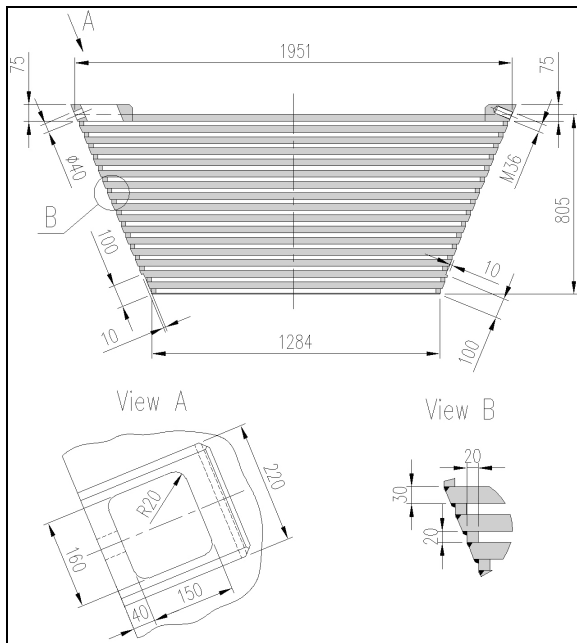

Fig. 16. Cross-section of the octagonal barrel beam.

The weight of the laminated yoke of solenoid is 305 ton. The weight of the carriage and of the space frames is about 16 ton. The weights of the yoke parts are given in the Table II. The total weight of the iron for the PANDA solenoid is 339 tons.

The procedure of the yoke and solenoid assembly doesn't differ from the procedure described in [1].
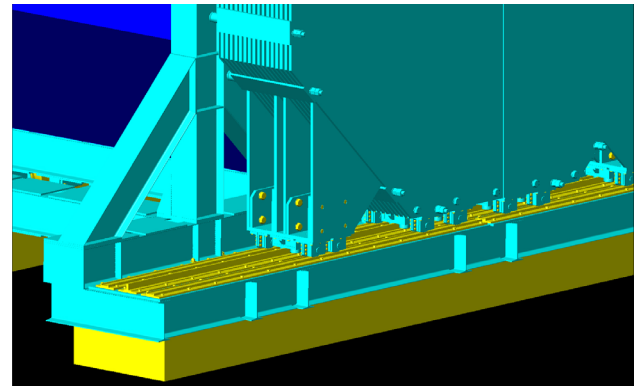

Fig. 17. Bottom part of the sliding doors.

TABLE II
THE WEIGHTS OF THE YOKE PARTS

	Weight, ton
DIRC's shield	
Inner cylinder	2,3
Butt washer	12,7
Barrel	19,7
Total:	**34,8**
Upstream end cap	
Coil mandrel	4,8
Solid washer	10,3
Total:	**15,1**
Octagonal barrel	
Upper beam	21,8
Inclined side beams (4 pcs.)	27,1
Vertical side beams (2 pcs.)	27,1
Bottom beam	25,0
Total:	209
Downstream door plus supports, space frames, wheels, rollers etc.	
Most heavy piece (of 4 pcs.)	20,5
Total:	**77,3**
Total weight of iron pieces:	**339**

REFERENCES

[18] Conceptual design report of JINR team. "2 T Superconducting Detector Solenoid for the PANDA Target Spectrometer, Part 1"

[19] F. Anulli et al. The muon and neutral hadron detector for BaBar. *Nuclear Instruments and Methods in Physics Research*, A 409 (1998), p.542

[20] J.Z.Bai et al. The BES detector. *Nuclear Instruments and Methods in Physics Research*, A344 (1994), p.319

[21] E.K. Koshurnikov, A.A. Efremov, Yu,Yu Lobanov, A.F. Makarov, H. Orth, A.N Sissakian, A.S. Vodopianov. Conceptual Design of the PANDA Magnet System. MT-19, *IEEE Transactions on Applied Superconductivity*, vol. 16, n. 2, 2006, p. 469-472.

[22] OPERA 3D – Software for Electromagnetic Design. TOSCA 9.0 Reference Manual. Vector Fields Ltd., Oxford, UK, 2003.

[23] COSMOS M v 2.95 User's Guide, System Research and Analysis Corp., Los Angeles, 2005.

[24] **"**Safety requirements of strength analysis of the equipment and pipe lines of nuclear power plants " *RF Regulation* PNAE G-7-002-86